



Monster Radio Jet (>66 kpc) Observed in Quasar at $z \sim 5$

Anniek J. Gloude1¹, Frits Sweij2², Leah K. Morabit2,3^{2,3}, Emanuele Paolo Farina4⁴, Kenneth J. Duncan5⁵Yuichi Harikane6⁶, Huub J. A. Röttgering7⁷, Aayush Saxena8⁸, and Jan-Torge Schindler9⁹¹NSF NOIRLab, Gemini Observatory, 670 North A'ohoku Place, Hilo, HI 96720, USA; [1@noirlab.edu">anniek.gloude1@noirlab.edu](mailto:anniek.gloude<span style=)²Centre for Extragalactic Astronomy, Department of Physics, Durham University, Durham DH1 3LE, UK³Institute for Computational Cosmology, Department of Physics, Durham University, Durham DH1 3LE, UK⁴International Gemini Observatory/NSF NOIRLab, 670 North A'ohoku Place, Hilo, HI 96720, USA⁵Institute for Astronomy, Royal Observatory, Blackford Hill, Edinburgh, EH9 3HJ, UK⁶Institute for Cosmic Ray Research, The University of Tokyo, 5-1-5 Kashiwa-no-Ha, Kashiwa City, Chiba, 277-8582, Japan⁷Leiden Observatory, Leiden University, P.O. Box 9513, 2300 RA Leiden, The Netherlands⁸Department of Physics, University of Oxford, Denys Wilkinson Building, Keble Road, Oxford OX1 3RH, UK⁹Hamburger Sternwarte, University of Hamburg, Gojenbergsweg 112, D-21029 Hamburg, Germany

Received 2024 September 6; revised 2024 November 12; accepted 2024 November 22; published 2025 February 6

Abstract

We present the discovery of a large extended radio jet associated with the extremely radio-loud quasar J1601+3102 at $z \sim 5$ from subarcsecond resolution imaging at 144 MHz with the International LOFAR Telescope. These large radio lobes have been argued to remain elusive at $z > 4$ due to energy losses in the synchrotron emitting plasma as a result of scattering of the strong cosmic microwave background at these high redshifts. Nonetheless, the $0''.3$ resolution radio image of J1601+3102 reveals a northern and a southern radio lobe located at 9 and 57 kpc from the optical quasar, respectively. The measured jet size of 66 kpc makes J1601+3102 the largest extended radio jet at $z > 4$ to date. However, it is expected to have an even larger physical size in reality due to projection effects brought about by the viewing angle. Furthermore, we observe the rest-frame UV spectrum of J1601+3102 with Gemini/GNIRS to examine its black hole properties, which results in a mass of $4.5 \times 10^8 M_{\odot}$ with an Eddington luminosity ratio of 0.45. The black hole mass is relatively low compared to the known high- z quasar population, which suggests that a high black hole mass is not strictly necessary to generate a powerful jet. This discovery of the first ~ 100 kpc radio jet at $z > 4$ shows that these objects exist despite energy losses from inverse Compton scattering and can put invaluable constraints on the formation of the first radio-loud sources in the early Universe.

Unified Astronomy Thesaurus concepts: [Radio loud quasars \(1349\)](#); [High-redshift galaxies \(734\)](#); [Radio jets \(1347\)](#)

1. Introduction

Despite the discovery of radio-loud¹⁰ quasars and radio galaxies up to $z \sim 7$ (e.g., I. D. McGreer et al. 2006; C. J. Willott & P. Delorme 2010; E. Bañados et al. 2015, 2021; A. Saxena et al. 2019; S. Belladitta et al. 2020; A. J. Gloude1 et al. 2022; R. Endsley et al. 2023), there appears to be a lack of large (\sim hundreds of kpc) radio lobes at $z > 4$ with the most extended radio jet measured to be 36 kpc at $z = 4.1$ (e.g., C. De Breuck et al. 1999; A. Saxena et al. 2024) and 1.6 kpc at $z \sim 6$ (E. Momjian et al. 2018). The lack of extended radio sources above $z > 4$ has previously been attributed to the cosmic microwave background (CMB) energy density, which increases with $(1+z)^4$ and causes energy losses of relativistic electrons in the radio jet by inverse Compton (IC) scattering (A. C. Fabian et al. 2014; G. Ghisellini et al. 2014). This effect causes high-redshift extended jets to become X-ray-bright and radio-weak. However, even with the most powerful X-ray telescopes, such as Chandra, it has been challenging to observe extended X-ray jets at $z > 4$ (see, e.g., T. Connor et al. 2021; L. Ighina et al. 2022).

The new generation of powerful radio telescopes, such as the Low Frequency Array (LOFAR; M. P. van Haarlem et al. 2013) and the near-future Square Kilometre Array (P. E. Dewdney et al. 2009), enables a combination of deep and wide-field imaging at frequencies of ~ 100 MHz for the first time. By combining the international LOFAR stations, a subarcsecond resolution (of $0''.3$) can be achieved at 144 MHz (see, e.g., E. Varenus et al. 2015; N. Ramirez-Olivencia et al. 2018; D. E. Harris et al. 2019; L. K. Morabito et al. 2022a; F. Sweij2 et al. 2022a, 2022b). This presents the opportunity to study distant radio sources at low frequencies in exquisite detail.

In this Letter, we present the discovery of a large (>66 kpc) extended radio jet at $z > 4$ for the first time using LOFAR long baseline imaging at $0''.3$ resolution. The resolved radio jet is associated with the extremely radio-loud quasar J1601+3102 at $z = 4.9$ that was discovered recently by A. J. Gloude1 et al. (2022) using the LOFAR Two-metre Survey Data Release 2 (LoTSS-DR2; T. W. Shimwell et al. 2022). In this work, we study its radio properties and derive its black hole properties from follow-up rest-frame UV spectroscopic observations using the Gemini Near-Infrared Spectrograph (GNIRS; J. H. Elias et al. 2006). The discovery of this source reveals the existence of extended radio sources into the cosmic dawn despite the increased CMB energy density. Throughout this work, we assume a Λ CDM cosmology with $H_0 = 70 \text{ km s}^{-1} \text{ Mpc}^{-1}$, $\Omega_M = 0.3$, and $\Omega_{\Lambda} = 0.7$ and use the AB magnitude system.

¹⁰ Quasars are classified as radio-loud when the radio-loudness $R > 10$, defined as $R = F_{5 \text{ GHz}}/F_{4400 \text{ \AA}}$ in the rest frame (K. I. Kellermann et al. 1989).

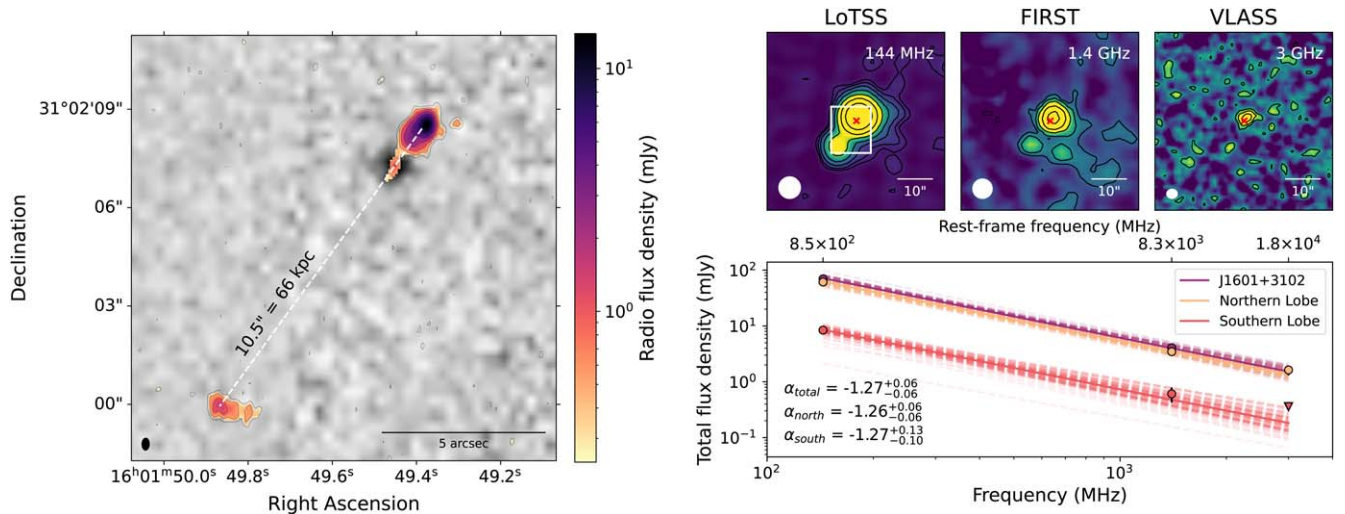


Figure 1. Left: LOFAR VLBI image of the extended radio jet of J1601+3102 at 144 MHz superimposed on an optical z -band image of the DESI Legacy Imaging Survey. The radio contours are drawn at $[-1, 1, 2, 4, 8, 16, 32] \times 3\sigma_{\text{rms}}$ with $\sigma_{\text{rms}} = 0.08 \text{ mJy beam}^{-1}$. The beam size (resolution of $0''.3$) is shown in the bottom left corner. The source shows a northern and a southern lobe at a distance of 1.4 and 8.9 from the optical quasar, which equals a projected distance of 9 and 57 kpc, respectively. The physical size of the extended radio jet is therefore $>66 \text{ kpc}$, making this the largest radio jet at $z > 4$ to date. Top right: low-resolution $50''$ radio cutouts from LoTSS, FIRST, and VLASS with radio contours drawn at $[-1, 0.5, 1, 2, 4, 8, 16, 32] \times 3\sigma_{\text{rms}}$. The respective beam sizes are indicated in the bottom left corner. The white rectangle corresponds to the LOFAR VLBI image in the left panel, and the red crosses indicate the position of the optical quasar. Bottom right: radio spectrum from 144 MHz to 3 GHz derived from these three radio surveys. The northern lobe is detected in all surveys; however, the southern lobe is only detected in LoTSS and FIRST. The nondetection in VLASS is given as a 3σ upper limit. The spectra are well described by a power law with the scatter indicated by the dashed lines. The spectral indices derived from these surveys are nearly identical with $-1.26_{-0.06}^{+0.06}$ and $-1.27_{-0.10}^{+0.13}$ for the northern and southern lobe, respectively.

Table 1
ILT Observation Setup

Property	Unit	Value
Central frequency	MHz	144
Frequency range	MHz	120–168
Pointing center	J2000	$\alpha = 16^{\text{h}}00^{\text{m}}28^{\text{s}}892$ $\delta = +30^{\circ}00'06''.911$
Integration time	s	1
Channel width	kHz	12.207
Observation time	s	28,800
Target distance	deg	1.07
Delay calibrator distance	deg	0.72
Target-delay calibrator sep.	deg	0.52

2. Data

The high- z quasar J1601+3102 was discovered as part of a sample of 20 radio-bright quasars, which were selected by combining an optical dropout selection with low-frequency radio observations (see A. J. Gloude-mans et al. 2022 for details). J1601+3102 stood out from this sample with an exceptionally high radio luminosity and steep spectral index. Therefore, to further explore its radio jet and supermassive black hole (SMBH) properties, we constructed a LOFAR very long baseline interferometry (VLBI) image at 144 MHz and observed the quasar with Gemini/GNIRS to obtain its (near-)infrared spectrum.

2.1. International LOFAR Telescope Data Reduction

The International LOFAR Telescope (ILT) data presented in this work were taken as part of the LoTSS (PI: Shimwell; project code LT10_010). Observations were carried out in the usual LoTSS fashion (T. W. Shimwell et al. 2022) consisting of a 10 minute observation of a flux density calibrator (3C 295,

L656058) followed by an 8 hr observation of the target field (P240+30, L656064). A total of 51 stations participated (24 core stations, 14 remote stations, 13 international stations). The observation setup is summarized in Table 1.

Data processing consisted of three parts: correcting for systematics, calibrating the Dutch array, and calibrating the international array. This was done using the LOFAR Initial Calibration (LINC; F. de Gasperin et al. 2019) pipeline for the systematics and for direction-independent calibration of the Dutch array. Calibration for the international array was done using the LOFAR VLBI pipeline (L. K. Morabito et al. 2022b) and `facetselfcal` (R. J. van Weeren et al. 2021). Calibration solutions were derived using DP3 (T. J. Dijkema et al. 2023). Imaging was done using `WSClean` (A. R. Offringa et al. 2014). Details of the full calibration procedure can be found in Appendix A.

The resulting LOFAR VLBI image ($\sigma_{\text{rms}} \sim 0.08 \text{ mJy beam}^{-1}$) is shown in Figure 1, which shows an extended radio jet with two lobes and core emission. We extract the source components and their flux densities using the Python Blob Detector and Source Finder (PYBDSF; N. Mohan & D. Rafferty 2015). Finally, to account for systematic offset in the flux calibration, a 10% flux density scale uncertainty is added in quadrature to the resulting flux density measurements. The radio structure, source association, and radio properties are discussed in Section 3.

2.2. Archival Radio Data

To obtain the radio spectral index¹¹ of the different components of J1601+3102, we utilize archival data from LoTSS-DR2, the Very Large Array (VLA) Faint Images of the Radio Sky at Twenty cm (FIRST) survey at 1.4 GHz (R. H. Becker et al. 1994), and the VLA Sky Survey (VLASS) at 2–4 GHz

¹¹ Defined as $S_{\nu} = \nu^{\alpha}$.

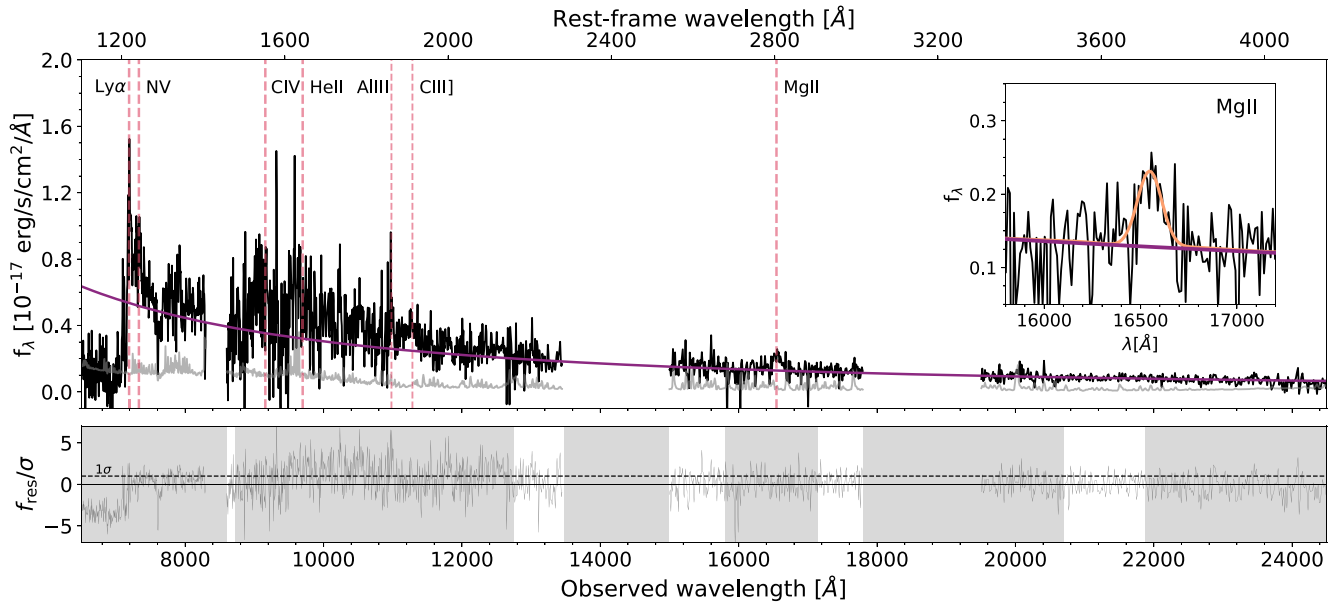


Figure 2. Top panel: composite optical and infrared spectrum of J1601+3102 obtained with HET/LRS2 ($<8500 \text{ \AA}$) and Gemini/GNIRS ($>8500 \text{ \AA}$) binned to a resolution of 200 km s^{-1} . The error of the GNIRS spectrum (gray) increases significantly toward bluer wavelengths. The continuum is described by a power law + iron pseudocontinuum (purple line; see Section 2.4). The wavelength regions heavily affected by telluric lines are masked for visualization purposes. The inset shows the Mg II line including the best fit with an FWHM of $2694^{+510}_{-383} \text{ km s}^{-1}$. Bottom panel: the residual flux divided by the error spectrum after subtracting the continuum and Ly α , N V, C IV, C III], and Mg II emission line fits (see Appendix B.1). The gray shaded regions show the masked regions for continuum fitting.

(M. Lacy et al. 2020). The available VLASS data for our source are an Epoch 3.1 Quick Look continuum image. J1601+3102 is detected in each of the three radio surveys, and their radio flux densities are again extracted using PYBDSF (see Section 3).

2.3. (Near-)infrared Spectroscopic Follow-up

The infrared spectrum of J1601+3102 was obtained with Gemini-North/GNIRS on 2024 March 19 (GN-2024A-FT-102; PI: Gloude-mans) using the cross-dispersed mode (32 lines mm^{-1}). This configuration provides wavelength coverage from 0.8 to $2.5 \mu\text{m}$ with a spectral resolution of $R \sim 650$, which allows for resolving the Mg II, C III], and C IV broad emission lines of the quasar. We observe J1601+3102 using the standard ABBA slit nodding technique ($3''$ offset) with a slit width of $0''.675$ and $0''.15$ pixel scale. The total time on target was 77 minutes with single exposures of 230 s each, resulting in five ABBA sequences. Preceding our science observation, we observe the standard star HIP 73156 (type A1V, $V=6.504 \text{ mag}$) for telluric correction and flux calibration. We reduce the data using the Python package Python Spectroscopic Data Reduction Pipeline (PYPEIT¹²; J. Prochaska et al. 2020a), which provides semiautomated reduction for spectroscopic data. Details of this reduction procedure are given in Appendix B.

We combine the reduced GNIRS spectrum with the optical spectrum obtained in A. J. Gloude-mans et al. (2022) with the Hobby Eberly Telescope LRS2 integral field spectrograph (HET/LRS2; L. W. Ramsey et al. 1998; G. J. Hill et al. 2021) in Texas, USA (see A. J. Gloude-mans et al. 2022 for details). The HET spectrum covers a wavelength range of $6450\text{--}10500 \text{ \AA}$ with a spectral resolution of $R \sim 1800$. We utilize the Python package SCULPTOR (J.-T. Schindler 2022) to create the composite spectrum and fit the continuum and emission lines (see Section 2.4 for details). We performed absolute flux calibration

on both the optical and infrared spectra using the Legacy DECam z -band magnitude of 21.19 ± 0.07 , since the quasar is not detected in existing wide-field near-infrared imaging surveys. We create the composite spectrum by normalizing the optical spectrum to the infrared spectrum. Finally, we rebin both spectra onto a common wavelength resolution of 200 km s^{-1} . The resulting spectrum used for analysis is shown in Figure 2, including a zoom-in on the detected Mg II broad emission line. In this figure, we masked the regions heavily affected by telluric contamination for visualization purposes.

2.4. Spectral Fitting

For our spectral fitting procedure of the rest-frame UV quasar spectrum, we again use the SCULPTOR package, considering both the continuum emission and broad emission lines. The continuum model generally consists of three components: a power law, Balmer pseudocontinuum, and iron pseudocontinuum. This method has been widely used and detailed in previous work for modeling quasar spectra (e.g., G. De Rosa et al. 2014; C. Mazzucchelli et al. 2017; Y. Shen et al. 2019; J.-T. Schindler et al. 2020; C. Bañados et al. 2021; E. P. Farina et al. 2022); therefore, we only provide a brief summary here.

The accretion disk emission is modeled with a normalized power law with slope α_λ at a rest-frame wavelength of 2500 \AA . We do not include a contribution from the Balmer continuum emission, because the spectral quality varies quite a bit, especially toward the bluer wavelengths. Finally, the iron contribution from the broad-line region, which is especially prominent around Mg II, is modeled using an empirical iron template of M. Vestergaard & B. J. Wilkes (2001) derived from a narrow-line Seyfert 1 galaxy, I Zwicky-1. To correctly model the iron emission in our spectrum, this iron template is broadened with the FWHM of our Mg II line. We fit this continuum model to wavelength regions free of emission lines, strong telluric absorption, and unusually large flux

¹² <https://github.com/pypeit/Pypeit>

errors: $\lambda_{\text{rest},o} = 1455\text{--}1475 \text{ \AA}$, $2155\text{--}2280 \text{ \AA}$, $2535\text{--}2675 \text{ \AA}$, $2900\text{--}3010 \text{ \AA}$, and $3500\text{--}3700 \text{ \AA}$.

We subtract the continuum model from the spectrum before fitting the broad emission lines. We fit the Ly α , N V, C IV, C III], and Mg II emission lines using a single Gaussian (see Appendix B.1). Because the Mg II fit and the iron contribution in the continuum model depend on each other, we iteratively fit both until the FWHM of the Mg II line converges.

To obtain confidence levels on these fitting parameters, we resample the observed spectrum 1000 times by assuming a Gaussian distribution of flux values centered around the measured flux value, with a standard deviation equivalent to the flux uncertainty, and refit each spectrum. The final best-fit parameters are given by the median of the distribution with 1σ uncertainties given by the 16th and 84th percentiles.

3. Large Extended Radio Jet

The LOFAR VLBI image of J1601+3102 reveals an extended radio structure including a northern radio lobe, a southern radio lobe, and a core (see Figure 1). The northern lobe is located at 1.4 from the optical quasar host (9 kpc projected distance) with a total flux density of 50.6 ± 5.1 mJy. The southern lobe is offset at 8.9 (57 kpc projected distance) with a total flux density of 10.5 ± 1.6 mJy.

3.1. Two Radio Lobes

To investigate whether the southern lobe is related to J1601+3102, we study the system's geometry, the radio spectra of both lobes, and the probability of misassociation. As a simple test, we connect the locations of the peak flux densities of both lobes. This line runs straight through the middle of the optical quasar host as shown in the left panel of Figure 1, which is the first indication that this could be the counterjet. In addition, the southern radio feature has the expected curved shape of a radio lobe propagating outward. To measure the spectral indices of radio features, we make use of the low-resolution archival radio data (see Section 2.2). The resulting low-frequency radio spectrum is displayed in the right panel of Figure 1. The southern lobe is not significantly detected in VLASS; therefore, a 3σ upper limit is given to constrain the spectral index. The spectral slopes of both lobes are remarkably similar, with slopes of $-1.26^{+0.06}_{-0.06}$ and $-1.27^{+0.13}_{-0.10}$ for the northern and southern lobe, respectively. The steepness and similarity of the two spectral indices are a strong indication that these both originate from J1601+3102, since steep slopes are often found in lobe-dominated radio galaxies (see, e.g., G. Miley & C. De Breuck 2008; C. Tadhunter 2016). The northern lobe does not show any evidence of a high-frequency break caused by an aging electron population in the radio lobes from the three data points (see, e.g., W. J. Jaffe & G. C. Perola 1973; M. Murgia 2003; J. R. Callingham et al. 2015). However, this could be due to the low number of measurements.

We note that there is a 3σ detected radio source in the FIRST image of 0.62 ± 0.22 mJy (see right panel of Figure 1), which is not detected in either LoTSS or VLASS. Given the local rms in those images, the spectral indices of this source are constrained to be $\alpha_{1.4\text{MHz}}^{1.4\text{GHz}} \geq 0.01$ and $\alpha_{1.4\text{GHz}}^{3\text{GHz}} \leq -0.7$, which indicates that it is possibly a faint gigahertz peaked spectrum (GPS) source. We suspect that this is either a GPS source unrelated to J1601+3102 or a noise spike (since the signal-to-noise ratio is $\lesssim 3$) and therefore do not include it in further analysis.

Finally, since there is no optical counterpart in any of the g -, r -, or z -band images of the DESI Legacy Imaging Survey (A. Dey et al. 2019) at the position of the southern lobe and no infrared counterpart detected in the W1-, W2-, W3-, and W4-band images of the Wide-field Infrared Survey Explorer (E. L. Wright et al. 2010) either, we calculate the probability that this radio source is associated with an optically faint radio galaxy below our detection limit. To determine this probability, we utilize the LoTSS Deep Fields data in the ELAIS-N1 and Lockman Hole fields (K. J. Duncan et al. 2021; R. Kondapally et al. 2021; J. Sabater et al. 2021; C. Tasse et al. 2021), which both reach a sensitivity of $\sim 20 \mu\text{Jy beam}^{-1}$ and have extensive multiwavelength coverage. To calculate the number density of >8 mJy radio galaxies below the 5σ detection limit of the Legacy surveys, we simply determine the number of galaxies in the multiwavelength catalogs of these fields that meet these criteria and divide that by the total survey area of 8.05 and 13.32 deg^2 for ELAIS-N1 and Lockman Hole, respectively. This results in an expected number of $\sim 9 \times 10^{-5}$ radio galaxies hiding within 100 arcsec^2 of our quasar. We do note that this calculation assumes a constant number density of galaxies, while quasars are known to reside in more strongly clustered environments (e.g., C. Garcia-Vergara et al. 2017). These faint optical galaxies typically have magnitudes of $\sim 23\text{--}26$ in the z band. The possible existence of such a source could therefore be confirmed with deep imaging. Combining all the previous arguments, we conclude that the southern radio feature is the counterjet of this quasar.

3.2. Physical Jet Properties

With a radio jet size of 66 kpc, J1601+3102 is the most extended radio jet ever observed at $z > 4$ (see Figure 3, right panel) with the largest previously known jets from a radio galaxy 36 kpc at $z = 4.1$ (e.g., C. De Breuck et al. 1999; L. Pentericci et al. 2000; A. Saxena et al. 2024) and other literature high- z quasars never exceeding ~ 2 kpc (E. Momjian et al. 2018). However, this projected jet size is only a lower limit, since its physical size is likely larger due to projection effects brought about by the viewing angle. The orientation-based unification scheme predicts that in the case of radio-loud quasars, the radio axis is oriented within 45° of the observer's line of sight (e.g., P. D. Barthel 1989; C. M. Urry & P. Padovani 1995). Considering a viewing angle $\theta > 45^\circ$ as measured from the radio axis to the plane of the sky, this would imply a lower limit on the physical jet size of >93 kpc.

The radio core is not resolved and has a total flux density of 2.2 ± 0.3 mJy. We calculate the brightness temperature of the different components using

$$T_b = \left(\frac{S_\nu}{\text{min} \times \text{maj}} \right) \times \left(\frac{1.22 \times 10^{12}}{\nu^2} \right) \times (1+z), \quad (1)$$

with S_ν the total flux density in janskys, ν the observed frequency in GHz, and min and maj the minor and major axis in milliarcseconds, respectively (see, e.g., L. K. Morabito et al. 2022a). Since the core is not resolved, we use the deconvolved size measurements to set a lower limit on T_b , which yields $T_b > 0.86 \times 10^7$ K. For the northern and southern lobes, we measure brightness temperatures of 6.3×10^7 K and 1.0×10^7 K, respectively, which is as expected above the typical active galactic nucleus (AGN) limit of $T_b \sim 10^{5-6}$ K at 144 MHz (L. K. Morabito et al. 2022a) and similar to the

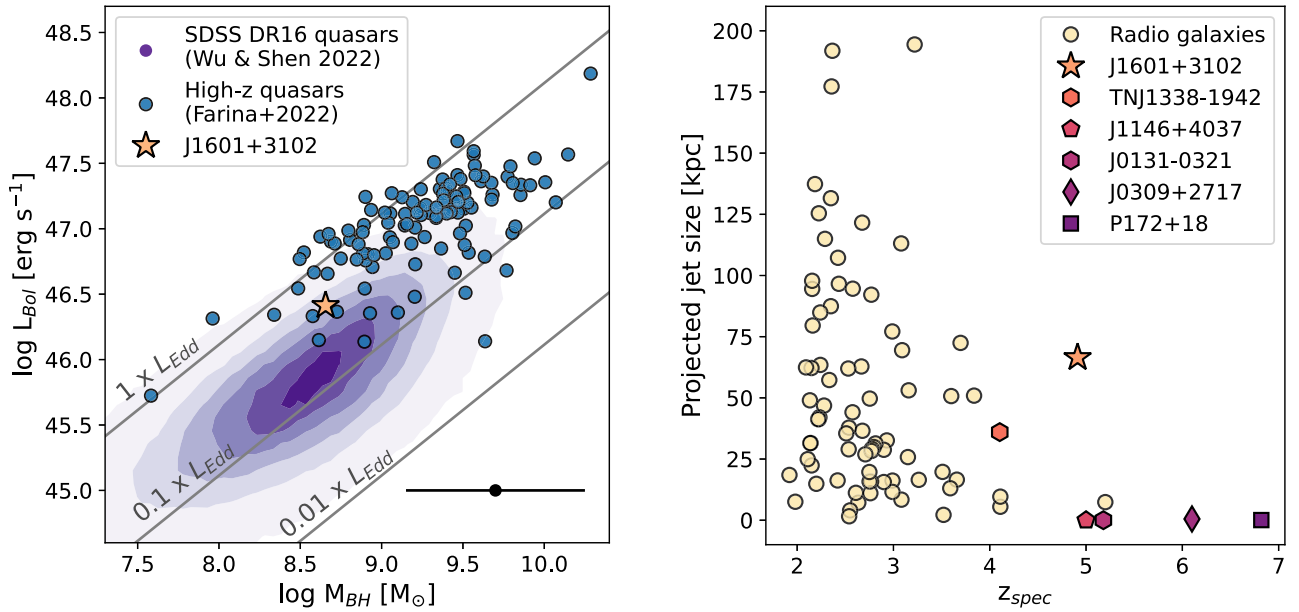


Figure 3. Physical properties of J1601+3102 compared to the literature. Left: black hole mass of J1601+3102 derived from the Mg II line vs. the bolometric luminosity compared to other known high- z quasars from E. P. Farina et al. (2022). The contours highlight the distribution of SDSS DR16 quasars in the range $0.27 < z < 2.72$ from Q. Wu & Y. Shen (2022). The systematic error on the black hole mass of ~ 0.55 dex is shown in the bottom right corner. The SMBH mass of J1601+3102 is lower than the average of this population, whereas the Eddington ratio is similar. Right: projected jet size of J1601+3102 compared to known high-redshift radio galaxies (A. Saxena et al. 2019) and quasars (J0309+2717, C. Spingola et al. 2020; P172+18, E. Momjian et al. 2021; J0131-0321/J1146+4037, Y. Shao et al. 2022). J1601+3102 is the first quasar at $z > 4$ with a large resolved radio jet.

resolved radio jet measurements of E. Momjian et al. 2018 at $z \sim 6$.

The radio lobes of J1601+3102 are highly asymmetric in terms of their brightness and distance from the quasar. As is apparent from Figure 1, the northern lobe is notably brighter (~ 5 times) and geometrically closer (~ 6 times) to the quasar. In general, the approaching hot spot is expected to be geometrically further away in the plane of the sky from the quasar since that lobe has been able to grow larger before the light from the receding jet arrives. The southern lobe is therefore likely the approaching jet, whereas the northern lobe is the receding jet. The apparent brightening of the northern lobe and asymmetry of the system are likely caused by the local environment, such as jet interaction with the (dense) interstellar medium (ISM; e.g., P. J. McCarthy 1991; N. P. H. Nesvadba et al. 2017; R. Dutta et al. 2024). This has been observed in other high- z radio galaxies as well, such as TN J1338-1942, where the southern lobe is about 3 times more distant than the northern lobe and ~ 4 times fainter (L. Pentericci et al. 2000). Follow-up observations (e.g., deep imaging or integral field unit) are necessary to measure the extended ionized gas around J1601+3102 and to confirm the environmental effects and jet-gas interaction that may be at play.

4. Black Hole Properties

We derive the black hole properties of J1601+3102 from the fitting routine described in Section 2.4. Specifically, we estimate the black hole mass using the FWHM of the Mg II line and the monochromatic luminosity using the empirical relation derived by Y. Shen et al. (2011) as

$$M_{BH} = 10^{6.74} \times \left(\frac{\text{FWHM}_{\text{Mg II}}}{1000 \text{ km s}^{-1}} \right)^2 \left(\frac{\lambda L_{\lambda, 3000}}{10^{44} \text{ erg s}^{-1}} \right)^{0.62}, \quad (2)$$

where λ is the wavelength and L_{λ} is the monochromatic luminosity at 3000 \AA . The uncertainty on the black hole mass is predominantly caused by the intrinsic scatter of this relation of ~ 0.55 dex. Furthermore, we calculate the bolometric luminosity using the relation of G. T. Richards et al. (2006) and Eddington luminosity given by

$$\begin{aligned} L_{bol} &= 5.15 \times \lambda L_{\lambda, 3000}, \\ L_{Edd} &= 1.3 \times 10^{38} \times M_{BH}. \end{aligned} \quad (3)$$

The results are summarized in Table 2. We obtain a black hole mass of $M_{BH} = (4.5^{+1.9}_{-1.2}) \times 10^8 M_{\odot}$ with a bolometric luminosity of $L_{bol} = (2.6 \pm 0.1) \times 10^{46} \text{ erg s}^{-1}$ an Eddington ratio $L_{bol}/L_{Edd} = 0.45^{+0.16}_{-0.13}$. We compare these results to the known high- z quasar population in Figure 3. This indicates that J1601+3102 is less massive than the general population but with a similar accretion rate, meaning J1601+3102 is currently in quasar mode and accreting efficiently. We also show the distribution of quasars in the range $0.27 < z < 2.72$ with Mg II line detections from the Sloan Digital Sky Survey (SDSS) Data Release 16 (DR16) quasar catalog (Q. Wu & Y. Shen 2022). To select only quasars with broad emission lines, we require $\text{FWHM}_{\text{Mg II}} > 1000 \text{ km s}^{-1}$. For consistency, we calculate their bolometric luminosity and black hole mass using Equations (2) and (3). Figure 3 shows that the black hole mass of J1601+3102 is comparable to the bulk of the low- z SDSS quasar sample. Lower-mass black holes (of $\sim 10^{6-8} M_{\odot}$) have also been found at high z with the discovery of faint AGN with JWST (see, e.g., Y. Harikane et al. 2023; R. Maiolino et al. 2023; D. D. Kocevski et al. 2024; J. Matthee et al. 2024). However, the black hole mass of J1601+3102 is still within the scatter of the high- z quasar population and therefore quite ordinary in comparison.

Table 2

Multiwavelength Measurements of J1601+3102 from This and Previous Work

R.A.	16:01:49.45
Decl.	+31:02:07.25
Optical Properties	
g, r, z	$>24.0, 23.15 \pm 0.13, 21.19 \pm 0.07$
W1, W2	$21.51 \pm 0.20, 21.31 \pm 0.35$
M_{1450}	$-24.75^{+0.31a}_{-0.21}$
α_λ	-1.71 ± 0.05
$\lambda L_{3000} \text{ \AA}$	$(5.0 \pm 0.1) \times 10^{45} \text{ erg s}^{-1}$
L_{bol}	$(2.6 \pm 0.1) \times 10^{46} \text{ erg s}^{-1}$
$z_{\text{Mg II}}$	$4.912^{+0.004}_{-0.005}$
$\text{FWHM}_{\text{Mg II}}$	$2694^{+510}_{-383} \text{ km s}^{-1}$
M_{BH}	$(4.5^{+1.9}_{-1.2}) \times 10^8 M_\odot$
$L_{\text{bol}} / L_{\text{Edd}}$	$0.45^{+0.16}_{-0.13}$
Radio Properties	
R_{2500}	520^{+310}_{-160}
R_{4400}	1020^{+720}_{-330}
$L_{150 \text{ MHz, tot}}$	$(2.8 \pm 0.4) \times 10^{28} \text{ W Hz}^{-1b}$
$S_{150 \text{ MHz, core}}$	$2.2 \pm 0.3 \text{ mJy}$
$S_{150 \text{ MHz, north}}$	$50.6 \pm 5.1 \text{ mJy}$
$S_{150 \text{ MHz, south}}$	$10.5 \pm 1.6 \text{ mJy}$
α_{total}	$-1.27^{+0.06}_{-0.06}$
α_{north}	$-1.26^{+0.06}_{-0.06}$
α_{south}	$-1.27^{+0.13}_{-0.10}$

Note.^a From A. J. Gloude-mans et al. (2022).^b Calculated using the LoTSS-DR2 total flux density of $69.8 \pm 7.7 \text{ mJy}$.

Using these black hole mass and Eddington ratio estimates, we can estimate the expected jet power of J1601+3102 in the thin disk regime, which is given by

$$Q_{\text{jet}} = 2 \times 10^{36} \left(\frac{M_{\text{BH}}}{10^9 M_\odot} \right)^{1.1} \left(\frac{\lambda_{\text{Edd}}}{0.01} \right)^{1.2} a^2 \text{ W}, \quad (4)$$

with λ_{Edd} the Eddington ratio and a the black hole spin (D. L. Meier 2002; Á. A. Orsi et al. 2016). To estimate the jet power, we assume $a = 1$, since radio-loud quasars are thought to have high black hole spin (e.g., L. Maraschi et al. 2012; A. Schulze et al. 2017). This calculation yields a jet power estimate of $(8^{+6}_{-4}) \times 10^{37} \text{ W}$ or $(8^{+6}_{-4}) \times 10^{44} \text{ erg s}^{-1}$. This is on the higher end of the predicted distribution of jet powers by A. Saxena et al. (2017).

5. Discussion

The large extended radio jet of J1601+3102 is unique because such a potentially $\sim 100 \text{ kpc}$ radio jet has never been found above $z > 4$ while being common at lower redshift ($z \sim 1-2$). The projected jet sizes of J1601+3102 and other known resolved quasars at $z > 4$ and radio galaxies at $z > 2$ are shown in the right panel of Figure 3. As discussed, the lack of extended radio sources in the early Universe has previously been attributed to the CMB energy density increasing with a factor of $(1+z)^4$, causing low-energy photons to be scattered to high energies by the IC effect. We also potentially see evidence of IC scattering in the LOFAR VLBI image of J1601+3102, since there seems to be a lack of diffuse radio emission between the two radio lobes (see Figure 1). Alternatively, it is possible that the diffuse emission may only be revealed at even lower

radio frequencies due to the steepness of the radio spectrum. Finally, we note that the high-resolution imaging process could have resolved out extended diffuse emission; however, since the source is relatively small and the flux density measurements at low and high resolution are similar, this is unlikely to be the main cause of the missing diffuse emission.

Interestingly, the SMBH of J1601+3102 is found to be lower mass compared to the average high- z quasar. Whether or not there is a correlation between the SMBH mass of quasars and their radio-loudness is still being debated in the literature, with studies both finding significant correlations (e.g., R. J. McLure & M. J. Jarvis 2004; N. Seymour et al. 2007; I. H. Whittam et al. 2022) and not finding them (e.g., G. Gürkan et al. 2019; C. Macfarlane et al. 2021; M. I. Arnaudova et al. 2024). Another recent study takes a new physically motivated approach to radio-loudness by separating the host galaxy star formation from the AGN contribution to the radio emission and finds that quasars hosting the 20% most massive SMBHs are 2–3 times more likely to host powerful radio jets than lower-mass SMBHs in otherwise similar quasars; however, quasars of all properties can still potentially host luminous jets (B. H. Yue et al. 2024). An exceptional Eddington accretion ratio is not strictly needed to generate powerful jets. We conclude that our finding of a relatively low SMBH mass is not in tension with the source exhibiting a huge bright radio jet, especially in the case of a high jet power (see Section 4).

The expected lifetime of the jets t can be approximated from the lobe length D , the gas density inside the lobe, and the jet power by simplifying Equation (A2) of C. R. Kaiser & Best (2007) to

$$D = C \left(\frac{Q_{\text{jet}}}{\rho} \right)^{1/5} t^{3/5}. \quad (5)$$

Assuming a constant gas density of $\rho = 10^{-22} \text{ kg m}^{-3}$ and a constant of $C = 1.7$ (see C. R. Kaiser & P. N. Best 2007) yields an age of $\sim 50 \text{ Myr}$ for a lobe size of 66 kpc . However, the physical lobe of J1601+3102 can be as large as 380 kpc for a viewing angle of $\theta = 80^\circ$, which would imply an age as high as $\sim 1 \text{ Gyr}$ and formation as early as $z \sim 10$. Note that the gas density is not expected to be constant around the radio source. Especially in the case of J1601+31, the environment is expected to play a crucial role in boosting the radio emission of the northern lobe; therefore, this age is only a simplified and crude estimate. Improving our understanding of systems like these is crucial to set observational constraints on the formation time of the first radio-loud sources in our Universe.

The average quasar lifetimes are not well constrained, with estimated duty cycles of $1 \text{ Myr}-1 \text{ Gyr}$ (e.g., P. Martini & D. H. Weinberg 2001; Q. Yu & S. Tremaine 2002; P. Martini 2004; Y. Shen et al. 2007). However, recent works using the He II proximity zone and quasar clustering suggest quasar accretion episodes of only a few Myr (e.g., I. S. Khrykin et al. 2021; E. Pizzati et al. 2024). This suggests that J1601+3102 could either be long-lived compared to the general quasar population or show recurrent quasar activity. However, there are no additional hot spots seen in the radio image, which is expected in the case of recurrent activity (e.g., L. Lara et al. 1999; S. Nandi et al. 2019).

The discovery in this work shows that these extended radio jets do exist at $z > 4$, and we speculate that the lack of extended jets at high z is (at least partly) due to selection effects. J1601+3102 has been discovered by selecting optical dropout

sources with low-frequency radio detections (see A. J. GlouDEMANS et al. 2022), whereas most radio-loud quasars are discovered at high radio frequencies from VLA observations at 1.4–5 GHz (e.g., R. Wang et al. 2007, 2008; E. Bañados et al. 2015; S. Belladitta et al. 2020). Since extended radio lobes are known to have steep spectral indices and therefore become brighter at low frequency, it is plausible that many of these extended radio sources have been missed in previous surveys. Furthermore, in previous work, high- z candidates have been selected on the basis of having compact morphologies (e.g., A. Saxena et al. 2019; K. Knowles et al. 2021). Due to the southern lobe of J1601+3102 not being connected to the northern component, it could easily be mistaken for a compact radio source. However, if the lobes had been slightly less extended, our source might have been classified as extended in the LoTSS-DR2 catalog (see right panel of Figure 1). This discovery therefore demonstrates that quasar and radio galaxy candidates could be incorrectly excluded from high- z searches that enforce the assumption that IC losses keep the extended lobes undetectable.

Finally, we note that the discovery of J1601+3102 demonstrates the existence of SMBHs in the early Universe with extremely efficient or energetic outflows. These could potentially influence the early quenching of galaxies, which have recently been found by JWST observations at similar redshift and point to the very early formation of massive galaxies (e.g., A. C. Carnall et al. 2023; T. J. Looser et al. 2024; T. Nanayakkara et al. 2024).

6. Summary

In this Letter, we present the discovery of a monster radio jet associated with the extremely radio-loud quasar J1601+3102 at $z \sim 5$ from subarcsecond-resolution imaging at 144 MHz. This radio jet is the largest yet identified at $z > 4$, with a size of >66 kpc. The $0''.3$ resolution LOFAR VLBI image shows that the radio emission is dominated by a northern and a southern lobe at a distance of $1''.4$ (9 kpc) and $8''.9$ (57 kpc) from the optical quasar, respectively, with steep radio spectral indices of -1.3 . The northern lobe is ~ 5 times brighter than the southern lobe and ~ 6 times closer to the nucleus of the quasar. This suggests that the northern lobe is potentially brightened by (extreme) interaction with the surrounding ISM and needs further investigation.

We detect the Mg II line in the quasar rest-frame UV spectrum, which gives an estimated black hole mass of $(4.5^{+1.9}_{-1.2}) \times 10^8 M_{\odot}$ and Eddington accretion ratio of $0.45^{+0.16}_{-0.13}$ with a bolometric luminosity of $L_{\text{bol}} = (2.6 \pm 0.1) \times 10^{46} \text{ erg s}^{-1}$. The black hole mass is lower than the general high- z quasar population, demonstrating that an exceptional mass is not strictly necessary to generate a powerful jet in this case. From the jet power, we approximate the expected lifetime of the jets of 50 Myr to ~ 1 Gyr. This age estimate is highly dependent on the gas density and the viewing angle, which determines the physical jet size. The determination of the viewing angle by, for example, X-ray observations is therefore necessary to pin down the physical size of the radio jet, the advance speed, and the age.

This quasar is unique, as it is the first quasar with large extended radio jets in the early Universe, which have remained elusive, potentially due to the increased CMB energy density at high redshift. The LOFAR VLBI image shows potential evidence of IC scattering because of the lack of diffuse radio emission between the two lobes. This work shows that these

large radio jets do exist at $z > 4$ but would easily be missed by selecting only at GHz frequencies and requiring compact morphologies. A combination of (blind) spectroscopic confirmation of new high- z radio-loud sources and VLBI observations is necessary to detect more of these monster radio jets in the early Universe and set constraints on the formation time of the first radio-loud sources.

Acknowledgments

The authors thank Philip Best for his valuable input to the discussion. F.S. is grateful for the support of STFC [ST/Y004159/1]. E.P.F. is supported by the international Gemini Observatory, a program of NSF NOIRLab, which is managed by the Association of Universities for Research in Astronomy (AURA) under a cooperative agreement with the U.S. National Science Foundation, on behalf of the Gemini partnership of Argentina, Brazil, Canada, Chile, the Republic of Korea, and the United States of America. L.K.M. is grateful for support from the Medical Research Council [MR/T042842/1]. J.T.S. is supported by the Deutsche Forschungsgemeinschaft (DFG, German Research Foundation) project number 518006966. K.J.D. acknowledges funding from the STFC through an Ernest Rutherford Fellowship (grant No. ST/W003120/1).

This Letter is based (in part) on data obtained with the International LOFAR Telescope (ILT) under project codes LC0 015, LC2 024, LC2 038, LC3 008, LC4 008, LC4 034, and LT10 01. LOFAR (M. P. van Haarlem et al. 2013) is the Low Frequency Array designed and constructed by ASTRON. It has observing, data processing, and data storage facilities in several countries, which are owned by various parties (each with their own funding sources) and collectively operated by the ILT foundation under a joint scientific policy. The ILT resources have benefited from the following recent major funding sources: CNRS-INSU, Observatoire de Paris, and Université d’Orléans, France; BMBF, MIWF-NRW, MPG, Germany; Science Foundation Ireland (SFI), Department of Business, Enterprise and Innovation (DBEI), Ireland; NWO, The Netherlands; The Science and Technology Facilities Council, UK; and the Ministry of Science and Higher Education, Poland.

Based on observations obtained at the international Gemini Observatory, a program of NSF NOIRLab, which is managed by the Association of Universities for Research in Astronomy (AURA) under a cooperative agreement with the U.S. National Science Foundation on behalf of the Gemini Observatory partnership: the U.S. National Science Foundation (United States), National Research Council (Canada), Agencia Nacional de Investigación y Desarrollo (Chile), Ministerio de Ciencia, Tecnología e Innovación (Argentina), Ministério da Ciência, Tecnologia, Inovações e Comunicações (Brazil), and Korea Astronomy and Space Science Institute (Republic of Korea).

This research made use of PYPEIT,¹³ a Python package for semiautomated reduction of astronomical slit-based spectroscopy (J. Prochaska et al. 2020a, 2020b).

Appendix A

ILT Calibration Procedure

A.1. Calibrating Systematics

The systematic corrections were obtained from the flux density calibrator observation using the LINC Calibrator

¹³ <https://pypeit.readthedocs.io/en/latest/>

pipeline. This finds and corrects for three effects in high band antenna observations. First, an average time-independent offset between the XX and YY correlations is taken out, as for an unpolarized source, no difference between the two is expected. Second, station bandpasses to convert correlator units to physical units are derived. Finally, an average clock offsets between all stations, and a reference station close to the center of the array is taken out. The remote and international stations have their own independent atomic clocks, which can drift approximately 20 ns per 20 minutes and thus are periodically synchronized to GPS (M. P. van Haarlem et al. 2013).

A.2. Direction-independent Calibration of Dutch Stations

The target observation is processed using the LINC Target pipeline, with the recently added self-calibration functionality. This first applies the corrections found by LINC Calibrator and corrects for ionospheric Faraday rotation using RMextract¹⁴ (M. Mevius 2018). Finally, the data are concatenated into a single frequency band, after which a phase-only calibration against a model from the Tata Institute of Fundamental Research Giant Metrewave Radio Telescope Sky Survey (TGSS) Alternative Data Release 1 (ADR1) is performed in order to correct for direction-independent ionospheric effects. At High Band Antenna frequencies, this is mainly a propagation delay (F. de Gasperin et al. 2019). DP3’s “smoothness constraint” was used to constrain the phase solutions to smooth behavior in the frequency domain over a running 5 MHz window. This was done to alleviate potential adverse effects from calibrating against the TGSS ADR1 model, which is less sensitive and has lower angular resolution than the ILT observations. An inner uv cut of 200λ was applied to match that of TGSS ADR1. Next, it makes an image of the field at $\sim 6''$ angular resolution using WSClean and does one round of phase-only self-calibration against the model obtained from that image.

A.3. International Station Calibration

Calibration of the international stations was done in three steps: calibration on a reference calibration source, self-calibration on the target source, and finally an astrometric correction on a nearby compact source with an identified optical counterpart.

Following the usual strategy (see, e.g., L. K. Morabito et al. 2022b; F. Swei-jen et al. 2022b), the international baselines were calibrated using a calibrator source in the Long Baseline Calibrator Survey (J. Moldón et al. 2015; N. Jackson et al. 2016, 2022), also referred to as a “delay calibrator.” Criteria for a good calibrator candidate are, for example, high flux density and compactness. For P240+30, the selected calibrator was ILT J155955.03+304223.7, a fairly compact source with a flux density, as measured in LoTSS, of $S_{\text{LoTSS}} = 1.0$ Jy, making it a prime calibration candidate. The visibilities were phase-shifted to the location of this source and subsequently averaged to a time resolution of 8 s and a frequency resolution of 390.625 kHz. Delay calibration was performed through self-calibration on this phase-shifted set of visibilities (see Table 3).

Due to the lack of an appropriate starting model, the self-calibration was started assuming a point source at the phase center of unit flux density. First, the data were converted from

Table 3
Delay Calibrator Self-calibration Parameters

Perturbation	Solution Interval	Smoothness Constraint (MHz)
scalarphasediff	4 minutes	10.0
scalarphase	8 s	1.25
scalarphase	8 s	10.0
scalarphase	60 s	10.0
scalarcomplexgain	1800 s	10.0
fulljones	1800 s	1.0

linear correlations to circular correlations. This makes correcting for Faraday rotation easier, as it will manifest as a phase difference between the parallel-hand RR and LL correlations, instead of moving signal into the cross-hand XY and YX correlations. The self-calibration procedure consisted of multiple cycles and several perturbations within each cycle. In the first four cycles, phase corrections were derived. From the fifth cycle on, when self-calibration had started to converge, amplitude corrections were also allowed. To reduce the impact of emission still seen on shorter baselines, an inner cut of $20k\lambda$ was used for the calibration. (N.B.: this was only used in the calibration aspect. No uv cut was used during imaging.) In summary, the following perturbations in facetsselfcal were used.

1. *Faraday rotation.* Using the `scalarphasediff` perturbation, a phase difference $\Delta\phi_{\text{FR}} = \phi_{\text{RR}} - \phi_{\text{LL}}$ was derived to capture the effects of Faraday rotation. This assumes that the source is not circularly polarized.
2. *Fast phases on international stations.* Using the `scalarphase` perturbation, polarization-independent phase corrections were derived for the international stations. Dutch station solutions were reset to zero phase (i.e., no correction), as those will be derived in the following perturbations.
3. *Residual fast phases on remote stations.* Using the `scalarphase` perturbation, polarization-independent phase corrections were derived for the remote stations. Solutions for the core stations were reset to zero phase, to be corrected in the next perturbation.
4. *Residual phases on core stations.* Using the `scalarphase` perturbation, polarization-independent phase corrections were derived for the core stations.
5. *Amplitude corrections.* Using the `scalarcomplexgain` perturbation, amplitude corrections were derived. These capture, e.g., residual bandpass corrections or errors in the primary beam model.
6. *Polarization corrections.* Using the `fulljones` perturbation, full-polarization corrections were derived for all four correlations. This corrects for leakage between the correlations under the assumption that the source is unpolarized.

In total, eight cycles of self-calibration were done using perturbations 1–5. After each calibration cycle, an image was made using a pixel size of 0.075 pixel^{-1} using a robust weighting of -1.5 .

A.4. Flux Density Scale

Amplitude solutions were normalized during self-calibration, preventing a major drift in the flux density scale. However, the

¹⁴ <https://github.com/lofar-astron/RMextract>

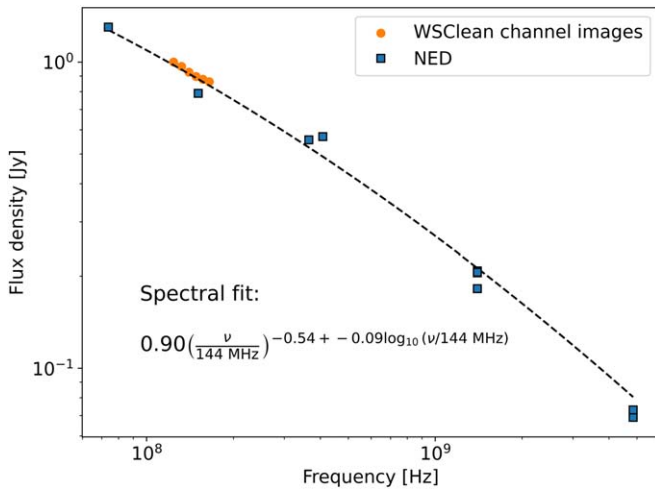


Figure 4. The fitted spectrum (dashed line) of the delay calibrator ILT J155955.03+304223.7, based on the photometry available in NED (squares) and the flux density as measured from the channel images output by WSClean (circles).

transfer of the bandpasses from the calibrator observation to the target field can still contain errors. Therefore, once self-calibration had converged, the CLEAN-component model was rescaled to the expected flux density and spectral index. The spectrum of the source was fitted using archival data points from the NASA Extragalactic Database (NED¹⁵). These were used to fit a flux density S_0 , a spectral index α_1 , and a spectral curvature α_2 using the form

$$S_\nu = S_0 \left(\frac{\nu}{\nu_{\text{ref}}} \right)^{\alpha_1 + \alpha_2 \log_{10} \nu / \nu_{\text{ref}}}, \quad (6)$$

where ν_{ref} is the reference frequency for which to derive the parameters. For our case, this was set to 144 MHz. The self-calibration of the delay calibrator was then repeated using the updated model as a starting model, except now all perturbations were solved only once, directly after each other, and a polarization correction was added to correct for leakage. The latter assumes that this source is unpolarized, which we base on the fact that it is not reported in the LoTSS-DR2 polarized source catalog of S. P. O’Sullivan et al. (2022). Figure 4 shows the fitted spectrum based on the photometry available in NED and the flux density as measured from the channel images output by WSClean. The flux density was measured in each channel by summing pixels within a $>5\sigma_{\text{rms}}$ region of the Stokes I image and dividing by the appropriate beam area in pixels.

A.5. Target Self-calibration and Astrometry

A new phase-shifted data set was created for J1601+3102, to which the final calibration solutions derived using the delay calibrator were applied. Notable direction-dependent effects

remain, as the target and delay calibrator are separated by $0''.5$ on the sky. These effects are dominated by ionospheric perturbations. Self-calibration on the target therefore provides a measure of the t_{ec} perturbation, which exploits the ionospheric perturbation’s functional form $\phi \propto d\text{TEC}/\nu$ to help constrain the solutions. The solution interval was calculated dynamically during the self-calibration cycles based on the signal detected on baselines $\gtrsim 148$ km. This gave a solution interval of approximately ~ 10 minutes.

An astrometric correction was derived using another compact radio source, ILT J160147.25+310222.4, which was near the main target and for which an optical counterpart had been identified in LoTSS-DR2. A compact source is preferred to reduce the ambiguity of determining the “center” of a source. CASA’s `imfit` task was used to fit a 2D Gaussian profile to this compact radio source in the subarcsecond-resolution ILT image. Using the centroid coordinates, the image was then shifted to match the optical coordinates. This correction was $0''.92$.

Appendix B (Near-)infrared Data Reduction

We reduced the data using PYPEIT¹⁶ (J. Prochaska et al. 2020a), which provides semiautomated reduction for spectroscopic data. The pipeline performed basic image processing on all 2D single exposures such as flat-fielding and cosmic-ray identification and masking (using the L.A. Cosmic Ray rejection algorithm; P. G. van Dokkum 2001). The images are then sky-subtracted using difference imaging between the AB dithered pairs and a 2D BSpline fitting procedure and wavelength-calibrated using the night sky lines. The 1D spectrum is automatically extracted from the 2D images using the optimal spectrum extraction procedure of K. Horne (1986). Before coadding the individual 1D spectra, the spectra are flux-calibrated using the standard star. The stacked spectrum is corrected for telluric absorption by fitting a model based on grids from the Line-By-Line Radiative Transfer Model (S. A. Clough et al. 2005; K. Gullikson et al. 2014).

B.1. Spectral Fitting

As discussed in Section 2.4, the Ly α , N V, C IV, and C III] emission lines are fitted with a single Gaussian after subtracting the continuum model, consisting of a power law and iron pseudocontinuum. A zoom-in on these emission lines and their best fits is shown in Figure 5. The resampling procedure (as outlined in Section 2.4) results in redshift values of $z_{\text{Ly}\alpha} = 4.920 \pm 0.002$ and $z_{\text{C IV}} = 4.866 \pm 0.008$ for the Ly α and C IV line, respectively. The C IV line of quasars is known to be often blueshifted with respect to the Mg II line due to outflows (e.g., C. M. Gaskell 1982). Our C IV and Mg II line fits result in a measured blueshift of $\Delta v_{\text{Mg II-C IV}} = 2350 \pm 450 \text{ km s}^{-1}$, which is close to the median value of $\Delta v_{\text{Mg II-C IV}} \sim 1850 \text{ km s}^{-1}$ found in the literature for quasars at $z \sim 6$ (J.-T. Schindler et al. 2020).

¹⁵ <https://ned.ipac.caltech.edu/>

¹⁶ <https://github.com/pypeit/Pypeit>

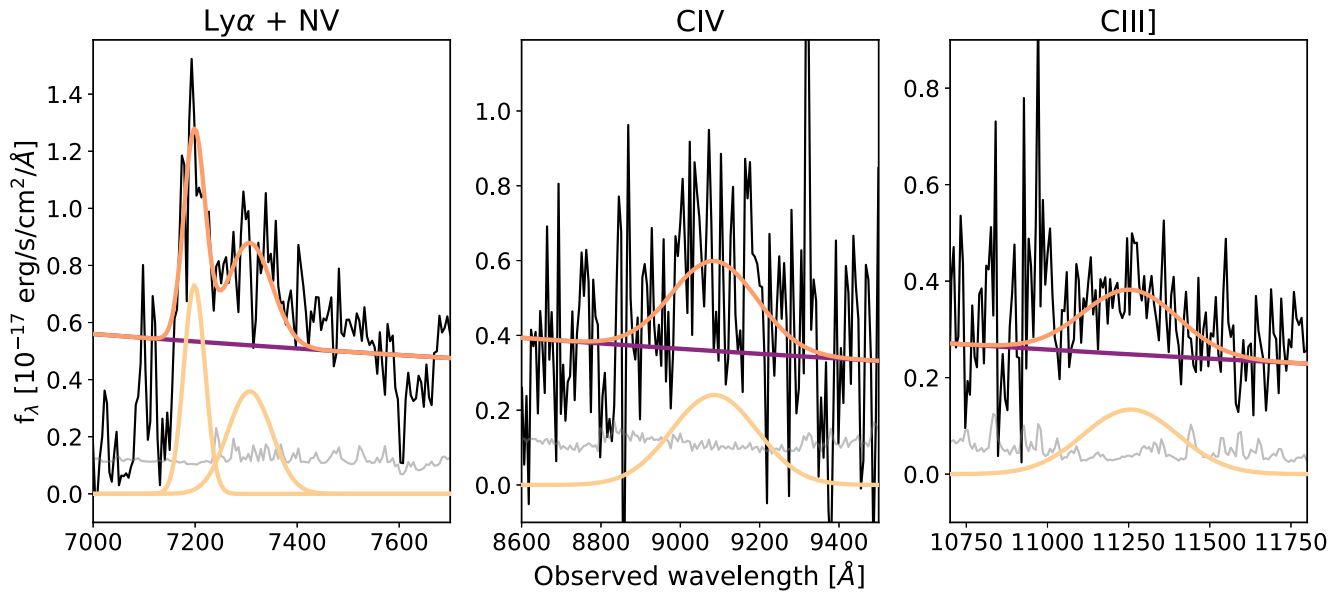


Figure 5. Zoom-in on the Ly α and N V emission lines (left), C IV line (middle), and C III] line (right). The spectrum is fitted using a power law and iron continuum (purple) and single Gaussian emission lines (yellow). The noise spectrum is indicated in gray.

ORCID iDs

Anniek J. GlouDEMANS <https://orcid.org/0009-0009-8274-441X>
 Frits Sweijen <https://orcid.org/0000-0002-6470-7967>
 Leah K. Morabito <https://orcid.org/0000-0003-0487-6651>
 Emanuele Paolo Farina <https://orcid.org/0000-0002-6822-2254>
 Kenneth J. Duncan <https://orcid.org/0000-0001-6889-8388>
 Yuichi Harikane <https://orcid.org/0000-0002-6047-430X>
 Huub J. A. Röttgering <https://orcid.org/0000-0001-8887-2257>
 Aayush Saxena <https://orcid.org/0000-0001-5333-9970>
 Jan-Torge Schindler <https://orcid.org/0000-0002-4544-8242>

References

- Arnaudova, M. I., Smith, D. J. B., Hardcastle, M. J., et al. 2024, *MNRAS*, **528**, 4547
- Bañados, E., Venemans, B. P., Morganson, E., et al. 2015, *ApJ*, **804**, 118
- Bañados, E., Mazzucchelli, C., Momjian, E., et al. 2021, *ApJ*, **909**, 80
- Barthel, P. D. 1989, *ApJ*, **336**, 606
- Becker, R. H., White, R. L., & Helfand, D. J. 1994, in ASP Conf. Ser. 61, *Astronomical Data Analysis Software and Systems III*, ed. D. R. Crabtree, R. J. Hanisch, & J. Barnes (San Francisco, CA: ASP), 165
- Belladitta, S., Moretti, A., Caccianiga, A., et al. 2020, *A&A*, **635**, L7
- Callingham, J. R., Gaensler, B. M., Ekers, R. D., et al. 2015, *ApJ*, **809**, 168
- Carnall, A. C., McLure, R. J., Dunlop, J. S., et al. 2023, *Natur*, **619**, 716
- Clough, S. A., Shephard, M. W., Mlawer, E. J., et al. 2005, *JQSR*, **91**, 233
- Connor, T., Bañados, E., Stern, D., et al. 2021, *ApJ*, **911**, 120
- De Breuck, C., van Breugel, W., Minniti, D., et al. 1999, *A&A*, **352**, L51
- de Gasperin, F., Dijkema, T. J., Drabent, A., et al. 2019, *A&A*, **622**, A5
- De Rosa, G., Venemans, B. P., Decarli, R., et al. 2014, *ApJ*, **790**, 145
- Dewdney, P. E., Hall, P. J., Schilizzi, R. T., & Lazio, T. J. L. W. 2009, *IEEEP*, **97**, 1482
- Dey, A., Schlegel, D. J., Lang, D., et al. 2019, *AJ*, **157**, 168
- Dijkema, T. J., Nijhuis, M., van Diepen, G., et al., 2023 DP3: Streaming Processing Pipeline For Radio Interferometric Data, Astrophysics Source Code Library, ascl:2305.014
- Duncan, K. J., Kondapally, R., Brown, M. J. I., et al. 2021, *A&A*, **648**, A4
- Dutta, R., Sharma, P., Sarkar, K. C., & Stone, J. M. 2024, *ApJ*, **973**, 148
- Elias, J. H., Joyce, R. R., Liang, M., et al. 2006, *Proc. SPIE*, **6269**, 62694C
- Endsley, R., Stark, D. P., Lyu, J., et al. 2023, *MNRAS*, **520**, 4609
- Fabian, A. C., Walker, S. A., Celotti, A., et al. 2014, *MNRAS*, **442**, L81
- Farina, E. P., Schindler, J.-T., Walter, F., et al. 2022, *ApJ*, **941**, 106
- García-Vergara, C., Hennawi, J. F., Barrientos, L. F., & Rix, H.-W. 2017, *ApJ*, **848**, 7
- Gaskell, C. M. 1982, *ApJ*, **263**, 79
- Ghisellini, G., Celotti, A., Tavecchio, F., Haardt, F., & Sbarrato, T. 2014, *MNRAS*, **438**, 2694
- GlouDEMANS, A. J., Duncan, K. J., Saxena, A., et al. 2022, *A&A*, **668**, A27
- Gullikson, K., Dodson-Robinson, S., & Kraus, A. 2014, *AJ*, **148**, 53
- Gürkan, G., Hardcastle, M. J., Best, P. N., et al. 2019, *A&A*, **622**, A11
- Harikane, Y., Zhang, Y., Nakajima, K., et al. 2023, *ApJ*, **959**, 39
- Harris, D. E., Moldón, J., Onk, J. R. R., et al. 2019, *ApJ*, **873**, 21
- Hill, G. J., Lee, H., MacQueen, P. J., et al. 2021, *AJ*, **162**, 298
- Horne, K. 1986, *PASP*, **98**, 609
- Ighina, L., Moretti, A., Tavecchio, F., et al. 2022, *A&A*, **659**, A93
- Jackson, N., Tagore, A., Deller, A., et al. 2016, *A&A*, **595**, A86
- Jackson, N., Badole, S., Morgan, J., et al. 2022, *A&A*, **658**, A2
- Jaffe, W. J., & Perola, G. C. 1973, *A&A*, **26**, 423
- Kaiser, C. R., & Best, P. N. 2007, *MNRAS*, **381**, 1548
- Kellermann, K. I., Sramek, R., Schmidt, M., Shaffer, D. B., & Green, R. 1989, *AJ*, **98**, 1195
- Khraykin, I. S., Hennawi, J. F., Worseck, G., & Davies, F. B. 2021, *MNRAS*, **505**, 649
- Knowles, K., Manaka, S., Bietenholz, M. F., et al. 2021, *Galax*, **9**, 89
- Kocevski, D. D., Finkelstein, S. L., Barro, G., et al. 2024, arXiv:2404.03576
- Kondapally, R., Best, P. N., Hardcastle, M. J., et al. 2021, *A&A*, **648**, A3
- Lacy, M., Baum, S. A., Chandler, C. J., et al. 2020, *PASP*, **132**, 035001
- Lara, L., Márquez, I., Cotton, W. D., et al. 1999, *A&A*, **348**, 699
- Looser, T. J., D'Eugenio, F., Maiolino, R., et al. 2024, *Natur*, **629**, 53
- Macfarlane, C., Best, P. N., Sabater, J., et al. 2021, *MNRAS*, **506**, 5888
- Maiolino, R., Scholtz, J., Curtis-Lake, E., et al. 2023, arxiv:2308.01230,
- Maraschi, L., Colpi, M., Ghisellini, G., Peregó, A., & Tavecchio, F. 2012, *JPhCS*, **355**, 012016
- Martini, P. 2004, in *Coevolution of Black Holes and Galaxies*, ed. L. C. Ho, 169 (Cambridge: Cambridge Univ. Press)
- Martini, P., & Weinberg, D. H. 2001, *ApJ*, **547**, 12
- Matthee, J., Naidu, R. P., Brammer, G., et al. 2024, *ApJ*, **963**, 129
- Mazzucchelli, C., Bañados, E., Venemans, B. P., et al. 2017, *ApJ*, **849**, 91
- McCarthy, P. J., van Breugel, W., & Kapahi, V. K. 1991, *ApJ*, **371**, 478
- McGreer, I. D., Becker, R. H., Helfand, D. J., & White, R. L. 2006, *ApJ*, **652**, 157
- McLure, R. J., & Jarvis, M. J. 2004, *MNRAS*, **353**, L45
- Meier, D. L. 2002, *NewAR*, **46**, 247
- Meivius, M., 2018 RMextract: Ionospheric Faraday Rotation Calculator, Astrophysics Source Code Library, ascl:1806.024
- Miley, G., & De Breuck, C. 2008, *A&ARv*, **15**, 67
- Mohan, N., & Rafferty, D., 2015 PyBDSF: Python Blob Detection and Source Finder, Astrophysics Source Code Library, ascl:1502.007.
- Moldón, J., Deller, A. T., Wucknitz, O., et al. 2015, *A&A*, **574**, A73
- Momjian, E., Bañados, E., Carilli, C. L., Walter, F., & Mazzucchelli, C. 2021, *AJ*, **161**, 207

- Momjian, E., Carilli, C. L., Bañados, E., Walter, F., & Venemans, B. P. 2018, *ApJ*, **861**, 86
- Morabito, L. K., Sweijen, F., Radcliffe, J. F., et al. 2022a, *MNRAS*, **515**, 5758
- Morabito, L. K., Jackson, N. J., Mooney, S., et al. 2022b, *A&A*, **658**, A1
- Murgia, M. 2003, *PASA*, **20**, 19
- Nanayakkara, T., Glazebrook, K., Jacobs, C., et al. 2024, *NatSR*, **14**, 3724
- Nandi, S., Saikia, D. J., Roy, R., et al. 2019, *MNRAS*, **486**, 5158
- Nesvadba, N. P. H., De Breuck, C., Lehnert, M. D., Best, P. N., & Collet, C. 2017, *A&A*, **599**, A123
- Offringa, A. R., McKinley, B., Hurley-Walker, N., et al. 2014, *MNRAS*, **444**, 606
- Orsi, Á. A., Fanidakis, N., Lacey, C. G., & Baugh, C. M. 2016, *MNRAS*, **456**, 3827
- O'Sullivan, S. P., Bruggen, M., & Vazza, F. 2022, yCat, IGMF limits with LOFAR (O'Sullivan+, 2020), Vizier On-line Data Catalog: J/MNRAS/495/2607. Originally published in:2020MNRAS.495.2607O
- Pentericci, L., Kurk, J. D., Röttgering, H. J. A., et al. 2000, *A&A*, **361**, L25
- Pizzati, E., Hennawi, J. F., Schaye, J., et al. 2024, *MNRAS*, **534**, 3155
- Prochaska, J., Hennawi, J., Westfall, K., et al. 2020a, *JOSS*, **5**, 2308
- Prochaska, J. X., Hennawi, J., Cooke, R., et al. 2020b, pypeit/Pypeit, v1.0.0, Zenodo, doi:10.5281/zenodo.3743493
- Ramírez-Olivencia, N., Varenus, E., Pérez-Torres, M., et al. 2018, *A&A*, **610**, L18
- Ramsey, L. W., Engel, L., Rhoads, B., et al. 1998, AAS Meeting Abstracts, **193**, 10.07
- Richards, G. T., Lacy, M., Storrie-Lombardi, L. J., et al. 2006, *ApJS*, **166**, 470
- Sabater, J., Best, P. N., Tasse, C., et al. 2021, *A&A*, **648**, A2
- Saxena, A., Röttgering, H. J. A., & Rigby, E. E. 2017, *MNRAS*, **469**, 4083
- Saxena, A., Röttgering, H. J. A., Duncan, K. J., et al. 2019, *MNRAS*, **489**, 5053
- Saxena, A., Overzier, R. A., Villar-Martin, M., et al. 2024, *MNRAS*, **531**, 4391
- Schindler, J.-T., 2022 Sculptor: Interactive Modeling Of Astronomical Spectra, Astrophysics Source Code Library, ascl:2202.018
- Schindler, J.-T., Farina, E. P., Bañados, E., et al. 2020, *ApJ*, **905**, 51
- Schulze, A., Done, C., Lu, Y., Zhang, F., & Inoue, Y. 2017, *ApJ*, **849**, 4
- Seymour, N., Stern, D., De Breuck, C., et al. 2007, *ApJS*, **171**, 353
- Shao, Y., Wagg, J., Wang, R., et al. 2022, *A&A*, **659**, A159
- Shen, Y., Strauss, M. A., Oguri, M., et al. 2007, *AJ*, **133**, 2222
- Shen, Y., Richards, G. T., Strauss, M. A., et al. 2011, *ApJS*, **194**, 45
- Shen, Y., Wu, J., Jiang, L., et al. 2019, *ApJ*, **873**, 35
- Shimwell, T. W., Hardcastle, M. J., Tasse, C., et al. 2022, *A&A*, **659**, A1
- Spingola, C., Dallacasa, D., Belladita, S., et al. 2020, *A&A*, **643**, L12
- Sweijen, F., Morabito, L. K., Harwood, J., et al. 2022a, *A&A*, **658**, A3
- Sweijen, F., van Weeren, R. J., Röttgering, H. J. A., et al. 2022b, *NatAs*, **6**, 350
- Tadhunter, C. 2016, *A&ARv*, **24**, 10
- Tasse, C., Shimwell, T., Hardcastle, M. J., et al. 2021, *A&A*, **648**, A1
- Urry, C. M., & Padovani, P. 1995, *PASP*, **107**, 803
- van Dokkum, P. G. 2001, *PASP*, **113**, 1420
- van Haarlem, M. P., Wise, M. W., Gunst, A. W., et al. 2013, *A&A*, **556**, A2
- van Weeren, R. J., Shimwell, T. W., Botteon, A., et al. 2021, *A&A*, **651**, A115
- Varenus, E., Conway, J. E., Martí-Vidal, I., et al. 2015, *A&A*, **574**, A114
- Vestergaard, M., & Wilkes, B. J. 2001, *ApJS*, **134**, 1
- Wang, R., Carilli, C. L., Beelen, A., et al. 2007, *AJ*, **134**, 617
- Wang, R., Carilli, C. L., Wagg, J., et al. 2008, *ApJ*, **687**, 848
- Whittam, I. H., Jarvis, M. J., Hale, C. L., et al. 2022, *MNRAS*, **516**, 245
- Willott, C. J., Delorme, P., Reylé, C., et al. 2010, *AJ*, **139**, 906
- Wright, E. L., Eisenhardt, P. R. M., Mainzer, A. K., et al. 2010, *AJ*, **140**, 1868
- Wu, Q., & Shen, Y. 2022, *ApJS*, **263**, 42
- Yu, Q., & Tremaine, S. 2002, *MNRAS*, **335**, 965
- Yue, B. H., Duncan, K. J., Best, P. N., et al. 2024, *MNRAS*, submitted